Epitaxial Thin-Film vs Single Crystal Growth of 2D Hofmann-Type Iron(II) Materials: A Comparative Assessment of their Bi-Stable Spin Crossover Properties

Carlos Bartual-Murgui,* Víctor Rubio-Giménez, Manuel Meneses-Sánchez, Francisco Javier Valverde-Muñoz, Sergio Tatay, Carlos Martí-Gastaldo, M. Carmen Muñoz, and Jose Antonio Real*

ABSTRACT: Integration of the ON−OFF cooperative spin crossover (SCO) properties of Fe^{II} coordination polymers as components of electronic and/or spintronic devices is currently an area of great interest for potential applications. This requires the selection and growth of thin films of the appropriate material onto selected substrates. In this context, two new series of cooperative SCO two-dimensional Fe^{II} coordination polymers of the Hofmann-type formulated $\{Fe^{II}(Pym)_2[M^{II}(CN)_4]\cdot xH_2O\}_n$ and $\{Fe^{II}(Isoq)_2[M^{II}(CN)_4]\}_n$ (Pym = pyrimidine, Isoq = isoquinoline; M^{II} = Ni, Pd, Pt) have been synthesized, characterized, and the corresponding Pt derivatives selected for fabrication of thin films by liquid-phase epitaxy (LPE). At ambient pressure, variable-temperature single-crystal X-ray diffraction, magnetic, and calorimetric studies of the Pt and Pd microcrystalline materials of both series display strong cooperative thermal induced SCO properties. In contrast, this property is only observed for higher pressures in the Ni derivatives. The SCO behavior of the $\{Fe^{II}(L)_2[Pt^{II}(CN)_4]\}_n$ thin films (L = Pym, Isoq) were monitored by magnetization measurements in a SQUID magnetometer and compared with the homologous samples of the previously reported isostructural $\{Fe^{II}(Py)_2[Pt^{II}(CN)_4]\}_n$ (Py = pyridine). Application of the theory of regular solutions to the SCO of the three derivatives allowed us to evaluate the effect on the characteristic SCO temperatures and the hysteresis, as well as the associated thermodynamic parameters when moving from microcrystalline bulk solids to nanometric thin films.

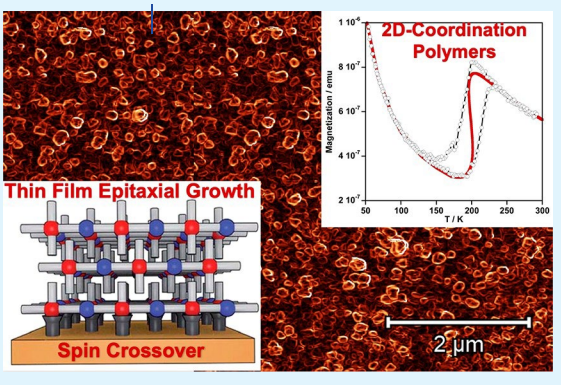

KEYWORDS: *spin crossover, Hofmann-type clathrates, coordination polymers, thin films, size-reduction effect, epitaxial growth*

INTRODUCTION

Switchable molecular materials have always attracted much attention since they are the origin of relevant physicochemical phenomena, but also because they are interesting platforms to explore potential applications in the areas of sensing, information storage, molecular actuators, and molecular electronic, and/or spintronic devices.[1,2]

Iron(II) SCO complexes are an important class of switchable molecular materials, which reversibly change between the paramagnetic (S = 2) high-spin (HS) and the diamagnetic (S = 0) low-spin (LS) electronic states.[3−9] The spin-state switch can be induced in a controlled mode through external perturbations such as temperature, pressure, light irradiation, or the inclusion of guest molecules. Moreover, the LS↔HS transitions can be easily detected following the inherent variation of several physical parameters such as dielectric constant,[10,11] magnetic moment,[6] structure,[12,13] and color/refractive index.[14,15] Hence, due to the reversible, controllable, and detectable characteristics of SCO, the introduction of this switchable property into chemical systems is presented as an outstanding opportunity for developing new smart materials.[16−18] In this conceptual framework, the design and synthesis of Hofmann-type two- and three-dimensional (2−3D) coordination polymers containing SCO-active Fe^{II} centers (Fe^{II}−HCPs) has motivated considerable research in the last two decades, thereby affording relevant examples of synergy between host−guest chemistry and SCO behavior.[5,19,20]

Of particular interest are the Fe^{II}−HCPs formulated $\{Fe^{II}(L)_x[M^{II}(CN)_4]\}$ where L is a bridging ditopic axial ligand (x = 1) or a terminal monotopic axial ligand (x = 2) and M^{II} = Pt, Pd, or Ni.[19] The Fe^{II} ions are equatorially connected through the

square-planar $[M(CN)_4]^{2-}$ anions yielding infinite $\{Fe^{II}[M^{II}(CN)_4\}_\infty$ 2D layers, which are linked either by coordination bonds through a bridging axial ligand or via $\pi-\pi$ intermolecular interactions between interdigitated terminal axial ligands thus affording 2D or 3D Fe^{II}–HCPs, respectively. Interestingly, these materials are amenable to being processed as thin films, opening the door to manufacture them as essential components of micro and nanosized SCO devices.[21] A highly explored thin film growing technique is LPE, which is a particular case of the layer-by-layer (LbL) method.[22−26] This process consists in successive immersions of a previously functionalized substrate into diluted solutions containing the precursors of the desired compound. This method was first validated for processing 3D Fe^{II}–HCPs which, excluding one case,[27] require very low temperatures (−60 °C) for achieving a regular epitaxial growth. Then, thin film fabrication was extended to 2D systems which were proved to be successfully grown at room temperature. This was demonstrated by Kitagawa and co-workers for ultrathin films (16 nm thick) of the 2D−Fe^{II}–HCPs system $\{Fe^{II}(Py)_2[Pt^{II}(CN)_4]\}$ (Py = pyridine, FePyPt) which, contrary to powder samples, display structural gate-opening accompanying the uptake of analytes.[28] More recently, an exhaustive characterization of the SCO property and its evolution with thickness reduction of ultrathin films of this compound was reported by us.[29] By using synchrotron X-ray absorption spectroscopy (XAS) studies we showed that films of FePyPt display SCO bahaviors similar to that of the microcrystalline sample above 15 layers. However, downsizing below this critical value resulted in a reduction of the cooperativity and completeness of the spin transition. Following the same bottom up approach we have recently reported the preparation and characterization of ultrathin films of two new 2D−Fe^{II}–HCPs formulated as $\{Fe(L)_2[Pt(CN)_4]\}$ [(L = pymidine (Pym, FePymPt) and isoquinoline (Isoq, FeIsoqPt)] (Scheme 1). This study was exclusively focused on the impact of the axial ligand over the structural flexibility and charge transport properties of the films.[30]

Scheme 1. Pyridine (Py), Pyrimidine (Pym), and Isoquinoline (Isoq) Axial Ligands Used for the 2D SCO $\{Fe(L_{ax})_2[M(CN)_4]\}$ Coordination Polymers

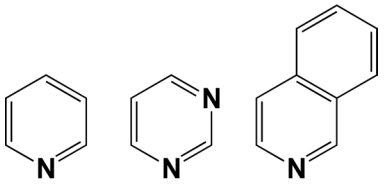

Here, we focus on the structure and SCO characterization of two new series of Fe^{II}–HCPs $\{Fe^{II}(Pym)_2[M^{II}(CN)_4]\}\cdot xH_2O$ [M^{II} = Pt and x = 0 (FePymPt), 0.5 (FePymPt·0.5H_2O), 1 (FePymPt·1H_2O); M^{II} = Pd and x = 0 (FePymPd), 1 (FePymPd·1H_2O); M^{II} = Ni and x = 0 (FePymNi)] and $\{Fe^{II}(Isoq)_2[M^{II}(CN)_4]\}$ [M^{II}= Pt(FeIsoqPt), M^{II} = Pd-(FeIsoqPd) and M^{II} = Ni(FeIsoqNi)] which were studied by single crystal X-ray diffraction, thermal-dependent magnetic susceptibility, and calorimetric measurements. Furthermore, thin films based on the tetracyanoplatinate counterparts of both systems were elaborated, and characterized by grazing incidence X-ray diffraction (GIXRD), X-ray photoelectron spectroscopy (XPS), and atomic force microscopy (AFM). Our study confirms the adequacy of the SQUID magnetometer measurements to assess the SCO in thin films above a threshold thickness value as previously proved for FePyPt. Indeed, the magnetic measurements unveil that, although the growth mechanism may depend on the axial ligand, overall, the single crystal to thin film transition provokes a drastic impact on the SCO properties.

RESULTS

Synthesis. Single crystals of FeLM·xH_2O [LM = PymPt (x = 0, 0.5, 1), PymPd (x = 0, 1), PymNi (x = 0), IsoqPt (x = 0), IsoqPd (x = 0), and IsoqNi (x = 0)] were obtained by slow diffusion of two aqueous solutions containing a mixture of Fe^{II}/Pym or Fe^{II}/Isoq (1:2.5) and $K_2[M^{II}(CN)_4]$ (M^{II} = Pt^{II} Pd^{II} or Ni^{II}) in a 1:1 ratio with respect to Fe^{II} (see the Experimental Section for more details). The reasonably good yields, ca. 50−60%, allowed us to carry out all physical characterizations from samples exclusively constituted of single crystals which were proved to be of a pure phase when comparing the experimental and simulated X-ray diffraction spectra (Supporting Information Figure S1). According to the crystallographic data (*vide infra*), Pt and Pd pyrimidine compounds crystallize with ca. one loosely attached molecule of water per Fe^{II} ion. Indeed, in the open air at room temperature FePymM·1H_2O (M = Pt, Pd) partially (M^{II} = Pt) or totally (M^{II} = Pd) lose the water molecule to give FePymPt·0.5H_2O or FePymPd. Furthermore, thermal treatment of FePymPt·0.5H_2O (i.e., 400 K during 30 min) affords complete dehydration to give FePymPt. However, this sample is hygroscopic and, hence, partially readsorbs water from air moisture (SI Figure S2).

SCO Properties. *Magnetic Measurements.* The thermal dependence of the $\chi_M T$ product (χ_M = molar magnetic susceptibility and T is the temperature) for FeLM·xH_2O was measured in the heating and cooling modes at 2 K min^{-1} for all derivatives. In order to avoid the desorption of the included water molecules, FePymPt·1H_2O and FePymPd·1H_2O were measured in their mother liquor. At room temperature, the $\chi_M T$ value is ca. 3.40 cm^3 K mol^{-1} for both compounds indicating that the Fe^{II} centers are essentially in the HS state (Figure 1a, b). This value remains almost constant upon cooling down to 202 K/212 K for Pt/Pd derivatives and below this temperature $\chi_M T$ abruptly drops reaching a value of 0.5 (Pt) and 0.4 (Pd) cm^3 K mol^{-1} at 160 K. This behavior is associated with a reversible strong cooperative and almost complete thermal spin transition with $T_{1/2}^{av} = (T_{1/2}^{\downarrow} + T_{1/2}^{\uparrow})/2$ = 221 (Pt) and 223 (Pd) K (being $T_{1/2}$ the temperature at which ΔG_{HL} = 0 when the HS and LS molar fractions of interconverted species are 0.5 and $T_{1/2}^{\downarrow}/T_{1/2}^{\uparrow}$ corresponding to the $T_{1/2}$ values derived from the cooling/warming modes). The hysteresis loops ($\Delta T_{1/2} = T_{1/2}^{\downarrow} - T_{1/2}^{\uparrow}$) are 41 (Pt) and 26 (Pd) K wide (see SI Table S1).

As mentioned above, crystals of FePymPt·1H_2O lose ca. half molecule of water at room temperature to afford FePymPt·0.5H_2O. This induces a narrowing of the hysteresis by 13 K ($\Delta T_{1/2}$ = 28.5 K), mainly affecting the cooling branch of the hysteresis, which moves from $T_{1/2}^{\downarrow}$ = 200 to 213 K, while the heating branch remains virtually unchanged ($T_{1/2}^{\uparrow}$ = 241.5 K). Then, according to the thermal analysis, this hemihydrate derivative was desolvated in situ in the SQUID magnetometer at 400 K for 30 min. The resulting FePymPt compound shows a cooperative spin transition centered at slightly higher temperatures ($T_{1/2}^{av}$ = 237 K, $\Delta T_{1/2}$ = 20.5 K) than those of the hemihydrate species. In contrast, desolvated compound

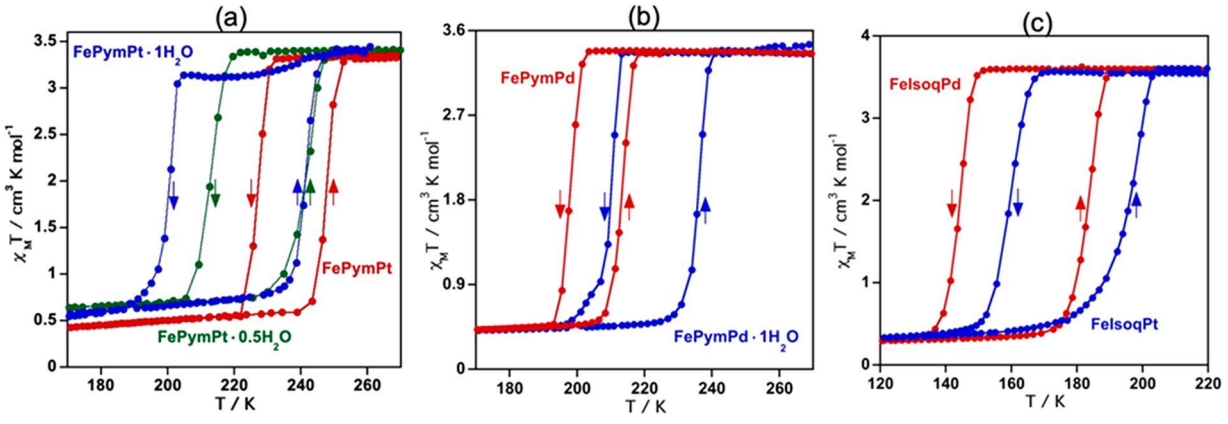

Figure 1. $\chi_M T$ vs T plots for: (a) FePymPt·xH$_2$O [x = 1 (blue), 0.5 (green) and 0 (red)]; (b) FePymPd·xH$_2$O [x = 1 (blue) and 0 (red)]; (c) FeIsoqM [M = Pd (red), Pt (blue)].

FePymPd, obtained from the spontaneous water desorption of FePymPd·1H$_2$O at room temperature, shows a cooperative SCO slightly shifted toward lower temperatures (with respect to the homologous solvate derivative) centered at $T_{1/2}^{av}$ = 206 K with $\Delta T_{1/2}$ = 15.4 K.

The SCO behavior of FeIsoqM (M = Pt, Pd) is similar to that found for the desolvated Pym derivatives but much more cooperative with average $T_{1/2}$ and $\Delta T_{1/2}$ equal to 178 and 36 K for FeIsoqPt and 164 and 39 K for FeIsoqPd (Figure 1c).

Given that the FePymNi and FeIsoqNi derivatives remain in HS at 10^5 Pa for the studied temperature range (2−300 K), we have investigated their magnetic behavior at higher pressures (see SI Table S1). For FePymNi, magnetic measurements were carried out at 10^5 Pa, 0.34, 0.50, and 0.74 GPa (Figure 2 up). At 10^5 Pa the thermal dependence of $\chi_M T$ is characteristic of a HS

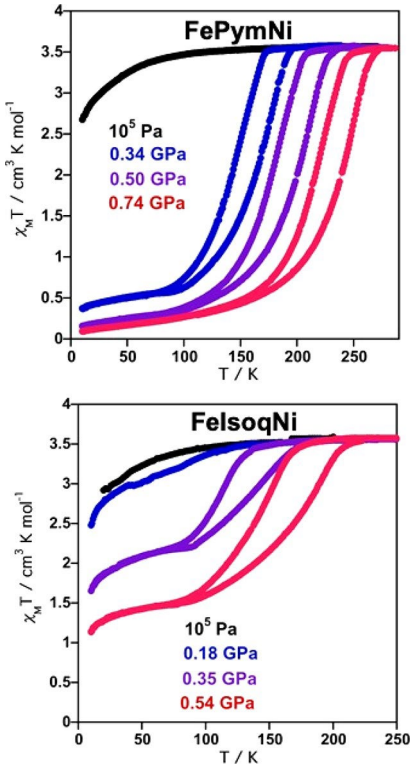

Figure 2. $\chi_M T$ vs T plots for FePymNi (up) and FeIsoqNi (down) at indicated pressures.

Fe^{II} compound with the low temperature region featuring the depopulation of the M_s microstates due to zero-field splitting of the S = 2 state. At 0.34 GPa, the compound clearly shows an almost complete cooperative SCO characterized by a thermal hysteresis, $\Delta T_{1/2}$, 21 K wide, despite this fact, the HS↔LS change is not very abrupt. The corresponding cooling and heating equilibrium temperatures are $T_{1/2}^{\downarrow}$ = 144 K and $T_{1/2}^{\uparrow}$ = 165 K ($T_{1/2}^{av}$ = 154.5 K). The SCO becomes practically complete at 0.5 and 0.74 GPa characterized by [$T_{1/2}^{\downarrow}$ = 176 K, $T_{1/2}^{\uparrow}$ = 198 K and $\Delta T_{1/2}$ = 22 K ($T_{1/2}^{av}$ = 187 K)] and [$T_{1/2}^{\downarrow}$ = 213.5 K, $T_{1/2}^{\uparrow}$ = 237.0 K and $\Delta T_{1/2}$ = 23.5 K ($T_{1/2}^{av}$ = 225 K)], respectively. For FeIsoqNi, the thermal dependence of $\chi_M T$ was investigated at 10^5 Pa, 0.18, 0.35, and 0.54 GPa (Figure 2 down). At 0.18 GPa the magnetic curve slightly deviates from the pure paramagnetic behavior denoting an incipient SCO behavior which is patent at 0.35 GPa. However, although cooperative, at this pressure it is rather incomplete with ca. 40% of transformation to the LS state and an estimated $T_{1/2} \approx$ 130 K. An additional 20% of conversion was observed at 0.54 GPa with $T_{1/2} \approx$ 154 K.

The pressure dependence of $T_{1/2}$ follows the Clapeyron relationship ($T_{1/2}(P) = T_{1/2} + P(\Delta V/\Delta S)$ with a slope equal to 179 K/GPa for FePymNi (SI Figure S3). For FeIsoqNi, even if there are only two points, the 163 K/GPa slope is also in the range observed for SCO complexes with linear dependence of $T_{1/2}(p)$ versus p.[31]

For both compounds, complete relaxation of pressure afforded the same paramagnetic behavior, indicating the complete reversibility of the measurements.

Calorimetric Measurements. Differential scanning calorimetry (DSC) measurements were performed in the heating and cooling modes to evaluate the SCO behavior of samples FePymPt·0.5H$_2$O, FePymPd, FeIsoqPt, and FeIsoqPd. The resulting ΔC_p versus T plots are depicted in SI Figure S4 together with the magnetic curves for comparison. Exothermic and endothermic anomalies were detected in the respective cooling and heating modes for all compounds and were associated to the corresponding SCO processes. The maxima/minima of these anomalies are placed at 211/234 K, 201/211 K, and 165/196 K, 147/187 K for FePymPt·0.5H$_2$O, FePymPd, FeIsoqPt, and FeIsoqPd, respectively, in quite good agreement with that observed with the magnetic measurements. The calculated enthalpy (ΔH) and entropy (ΔS) average variations related to the spin transitions are ΔH_{av} = 16.5 (FePymPt·0.5H$_2$O), 14.6 (FePymPd), 10 (FeIsoqPt), and 11.2 (FeI-

soqPd) kJ·mol^{-1}; ΔS_{av} = 74 (FePymPt·0.5H_2O), 70.8 (FePymPd), 55.1 (FeIsoqPt), and 60.5 (FeIsoqPd) J·K^{-1}·mol^{-1}. These values are in the range of those expected for spin transitions in cyanide bridged Fe^{II} compounds.[19]

Structural Analysis. Single crystal X-ray diffraction measurements were performed for the LS/HS configurations of FePymPt·0.5H_2O (180/260 K), FePymPd·1H_2O (120/250 K), FeIsoqPt and FeIsoqPd (120/220 K). The structure of the FePymNi and FeIsoqNi derivatives were determined at 120 and 100 K, respectively. Relevant crystallographic parameters are gathered in SI Tables S2 and S3.

Structure of FePymPt·0.5H_2O and FePymPd·1H_2O. At 180/120 K, the isostructural crystals of FePymPt·0.5H_2O/FePymPd·1H_2O are dark red and present the orthorhombic *Cmmm* space group. Representative bond lengths and angles are collected in SI Table S4. The structure consists of a crystallographically unique Fe^{II} center featuring a [Fe$^{II}N_6$] octahedral site whose axial positions are coordinated by two equivalent Pym rings. These act as terminal monotopic ligands while the equatorial positions are filled with four cyanide groups belonging to four equivalent [M(CN)$_4$]$^{2-}$ anions (Figure 3a). The average Fe−N

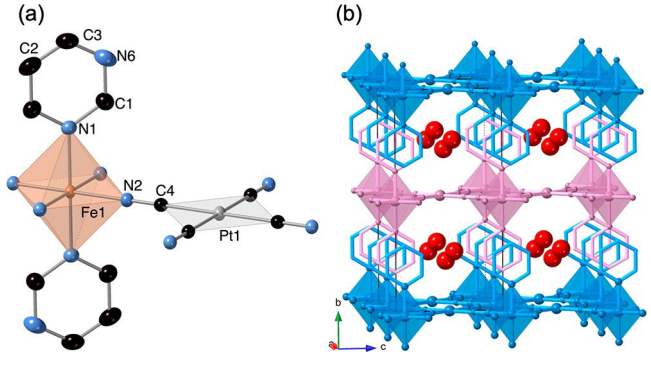

Figure 3. (a) Perspective view of a representative fragment displaying the Fe^{II} environment of complex FePymM·xH$_2$O (M = Pt (x = 0.5) and Pd(x = 1)), N6, and C2 atoms are related by symmetry and have 0.5 occupancy factor. (b) Packing of three equivalent layers highlighted in pink and blue. Red spheres represent the adsorbed water molecules.

distances of 1.955/1.961 Å (Pt/Pd) are consistent with a Fe^{II} ion in the LS configuration, in good agreement with the magnetic data. At 260/250 K the crystals maintain the same space group but the color changes to pale-yellow indicating a switch to the HS state. This is confirmed by the average Fe−N bond length of 2.164/2.155 Å (Pt/Pd), ca. 0.2 Å larger than observed for the LS state thereby making the distortion of the elongated HS octahedrons more noticeable. In both states and for symmetry reasons, static disorder was modeled in two equivalent positions with 0.5 occupancy for the noncoordinated nitrogen atom and shared carbon atoms of Pym.

The octahedrons are interconnected through the four arms of the square planar [M(CN)$_4$]$^{2-}$ anions defining strictly planar {Fe(Pym)$_2$[M(CN)$_4$]}$_\infty$ layers, which extend parallel to the *a*-*c* plane with the Pym ligands lying in the *b*-*c* plane and protruding along *b*. There, the layers stack in such a way that the Pym ligands of one layer point just to the middle of the {Fe$_2$[M(CN)$_4$]$_2$} square windows of the two adjacent layers. The interlayer separation is around 7.35 and 7.56 Å in the LS and HS state, respectively. The interdigitated Pym ligands display weak $\pi\cdots\pi$ intermolecular interactions with centroid-to-centroid distances in the 3.73−3.61 Å interval (Figure 3b).

Interstitial electronic density was observed and assigned to the presence of ca. 0.5 (for FePymPt·0.5H_2O) and 1 (for FePymPd·1H_2O) molecules of water per Fe^{II} ion. These water molecules are located within the channels along the *a* axis (Figure 3b) and interact with the non-coordinated nitrogen atom of the pyrimidine ligand defining H-bonds ranging in the interval 2.835(6)-3.004(6) Å (SI Figure S5). Indeed, the thermal dependence of the unit cell volume agrees reasonably well with the SCO obtained from the magnetic behavior of FePymPt·0.5H_2O and FePymPd·1H_2O (see SI Figure S6). Hence, the observed modifications of the magnetic curves associated to the desorption of the water molecules (see magnetic measurements section) reflect the interplay between the SCO and the host−guest interactions displayed by these clathrates. Unfortunately, the loss of crystallinity upon complete desorption of water prevented us to determine the crystal structures of FePymPt and FePymPd. However, the resemblance of the powder X-ray diffraction patterns corresponding to the solvated and unsolvated counterparts (SI Figure S7) exclude the occurrence of important structural changes associated to the solvent desorption.

Structure of FePymNi. The FePymNi yellow crystals belong to the orthorhombic *Pnma* space group at 120 K. Although the coordination environment of Fe^{II} is similar to that described for the Pt/Pd derivatives, there are notable structural differences in the Ni^{II} complex (Figure 4): (i) the axial pyrimidine ligands are

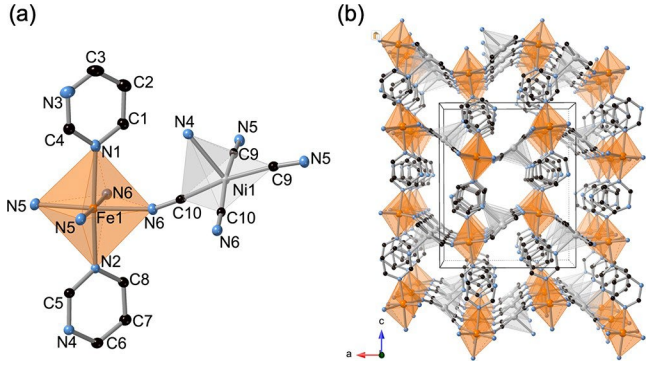

Figure 4. (a) Perspective view of a representative fragment displaying the Fe^{II} environment of FePymNi and (b) its three-dimensional framework with sqp topology.

not crystallographically equivalent, one acts as monotopic ligand while the other acts as ditopic ligand; (ii) the coordination environment of Ni^{II} is not a [NiC$_4$] square planar anymore but [NiC$_4$N] square pyramidal due to the elongated axial coordination of the Ni^{II} center by the N4 atom of the ditopic Pym; (iii) as a consequence, the 2D {Fe[Ni(CN)$_4$]}$_\infty$ layers are strongly corrugated defining an angle of 147.82° between the equatorial plane [Fe(N$_{eq}$)$_4$] and the average [NiC$_4$] plane. The interaction between layers defines a 3D five connected network with distorted sqp topology (SI Figure S8).[32,33] The average Fe−N bond length (2.165 Å) indicates a HS configuration consistent with the magnetic observations. The axial Ni^{II}−N$_4$ bond length is 2.399(3) Å while the equatorial bond lengths Ni−C9 and Ni−C10 are 1.863(3) and 1.870(3), respectively.

Structure of FeIsoqM (M = Pt, Pd, Ni). Compounds FeIsoqM (M = Ni, Pd, Pt) have been found to be isostructural. All of them display the triclinic *P*-1 space group regardless of the spin state (Figure 5a, b). Representative bond lengths and angles are collected in SI Table S5. At 120 K, crystals of FeIsoqPt and

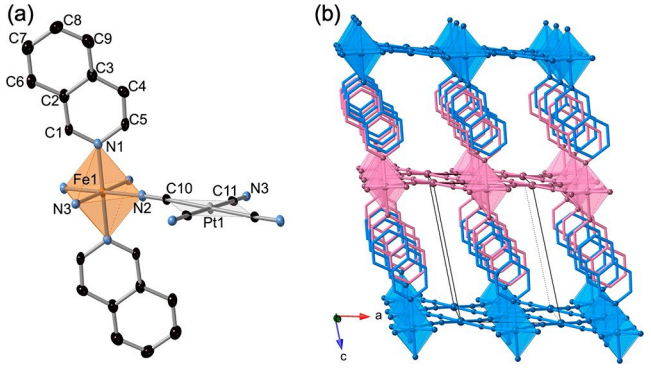

Figure 5. (a) View of the Fe^{II} environment of complex FeIsoqM (M^{II} = Pt, Pd, Ni). (b) Packing of three successive 2D layers highlighted in pink and blue.

FeIsoqPd are dark red (LS), whereas those of FeIsoqNi are pale yellow (HS), thus reflecting the spin state of the Fe^{II} center. Accordingly, the average Fe−N bond length are 1.967 (Pt), 1.961 (Pd), and 2.174 (Ni) Å, in good agreement with the $\chi_M T$ value at the same temperature. The structure, constituted of $\{Fe(Isoq)_2[M(CN)_4]\}_\infty$ layers stacked along the [001] direction (see Figure 5b), is in general terms similar to that of FePymM·$x$$H_2O$ (M = Pt, Pd). In the LS state, the layers are practically planar with a separation between consecutive layers of 9.439 Å for M = Pt and 9.416 Å for M = Pd. The protruding Isoq ligands of adjacent layers interdigitate defining weak $\pi\cdots\pi$ intermolecular contacts with an average separation of 3.68(2) Å (Pt, Pd).

At 220 K, FeIsoqPt and FeIsoqPd become pale yellow and the average Fe−N bond length increases by 0.209 (Pt) and 0.215 (Pd) denoting a complete LS-to-HS transformation. Concerning the $\pi\cdots\pi$ contacts, the average distance between Isoq ligands display a more moderate increase by ca. 0.1 Å. For the three Isoq derivatives, the layers are notably corrugated in the HS state. Indeed the angle defined between the equatorial $[FeN_4]_{eq}$ and $[M(CN)_4]^{2-}$ planes deviates 25−29°. This deviation is only 9−10° in the LS state for the Pt and Pd derivatives. This change of layer corrugation upon spin state switch influences the tilt angle of the axial Isoq ligands which changes from 15−16.5° in the HS state to ca. 6° in the LS state with respect to the normal direction of the (a,b) plane which contains the Fe and Pt centers (see SI Figure S8). Although to a very small extent, this fact also slightly influences the separation between the layers, being ca. 0.1 Å smaller in the HS state. A direct consequence is that the relative

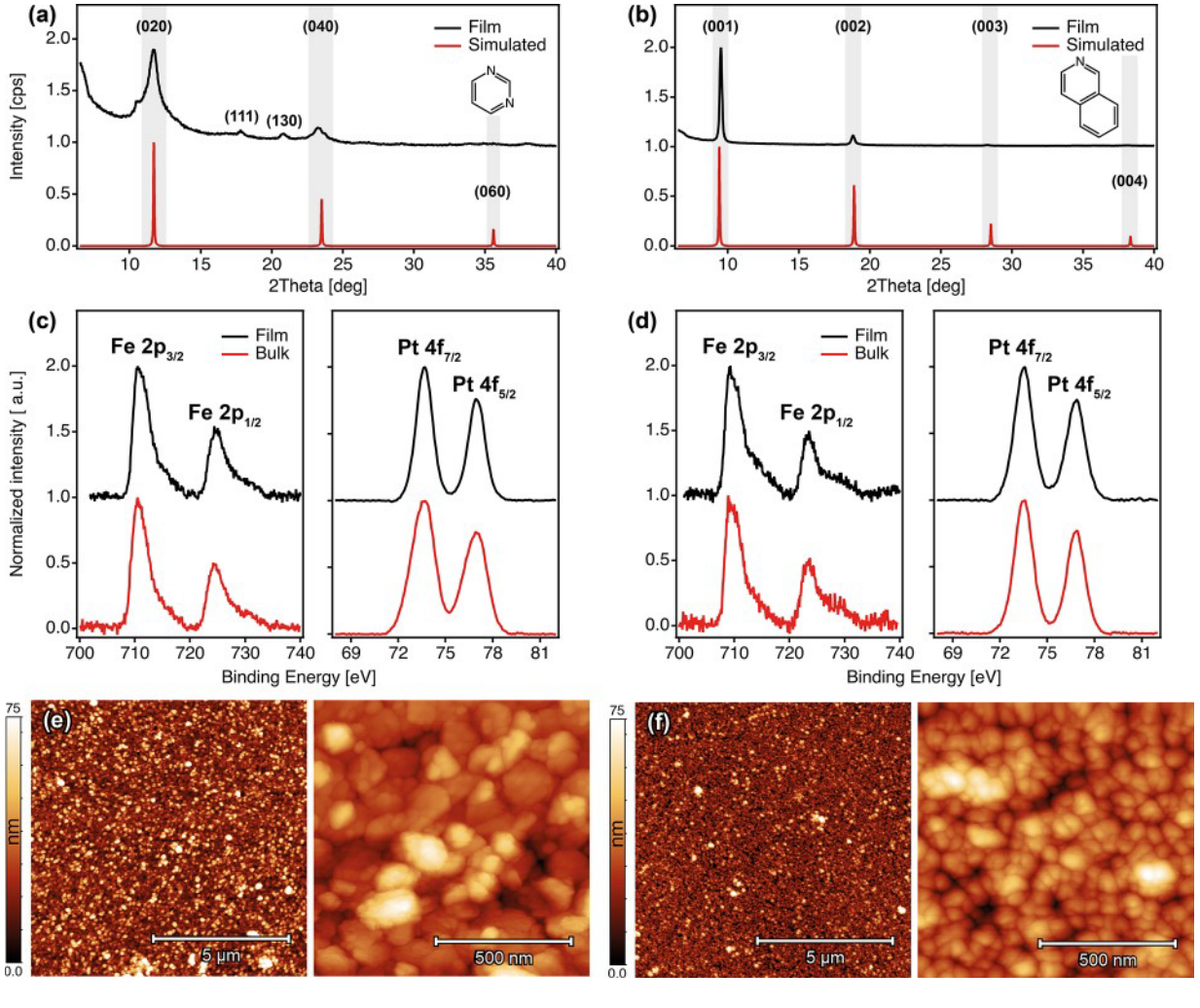

Figure 6. Characterization of FeLPt thin films (L = Pym, Isoq). Out-of-plane GIXRD diffractograms of L = Pym (a) and Isoq (b) thin films together with their respective simulated profiles. Gray panels highlight the most intense diffraction lines. High-resolution XPS spectra of the Fe 2p and Pt 4f regions for Pym (c), and Isoq (d) thin films. 10×10 and 1 × 1 μm^2 AFM topography images of L = Pym (e) and Isoq (f) thin films.

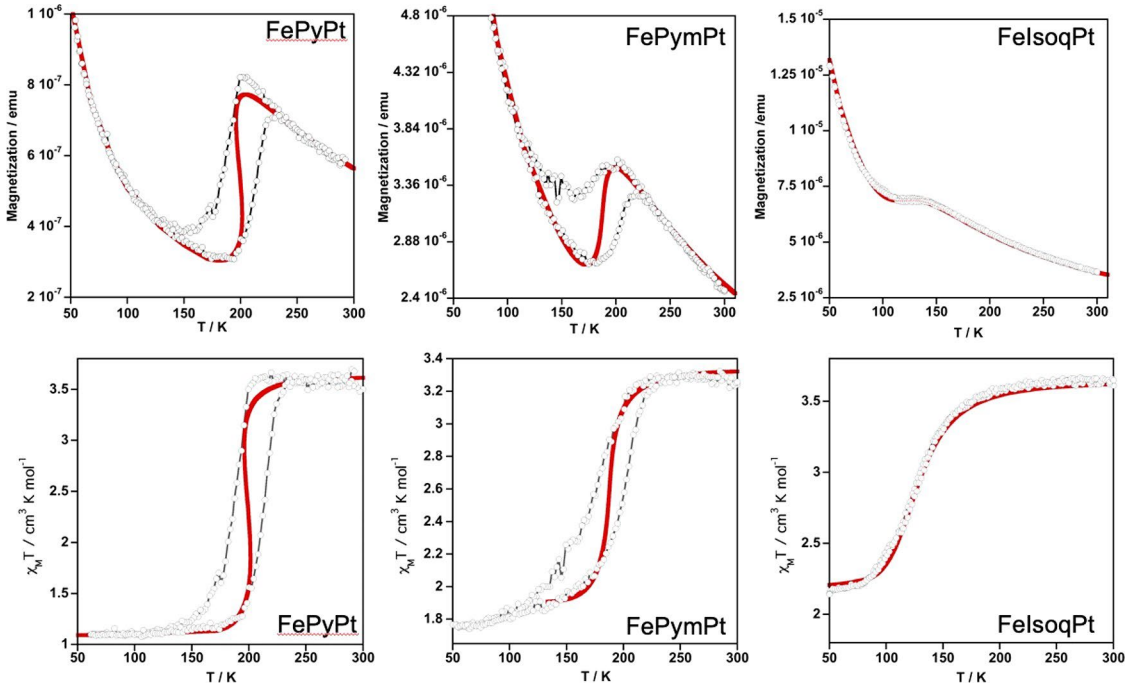

Figure 7. SCO properties of the thin films represented as the thermal dependence of the magnetization (top) and the product $\chi_M T$ vs T (down), being χ the magnetic susceptibility for the whole mass contained in the film and T temperature. Solid red lines correspond to the simulated magnetic behaviors.

change of the unit cell volume upon SCO, $\Delta V_{SCO}/V_{HS}$ = 5.12%, is markedly smaller than observed for the Pym derivatives (10.12%).

Epitaxial Growth of SCO Thin Films. Thin films of FePymPt and FeIsoqPt were synthesized using the LPE method following our previous work.[29,30] The LPE procedure entails the sequential assembly of the precursors in solution, that is, Fe^{II}, $[Pt(CN)_4]^{2-}$ and L (L = Pym or Isoq), onto a Au substrate previously functionalized with a 4-mercaptopyridine (py-SH) self-assembled monolayer (SAM). This SAM guides the film growth either by coordination to Fe^{II} or by $\pi\cdots\pi$ interactions with adjacent axial ligands (see more details in the Experimental Section). As previously demonstrated for thin films of FePyPt,[29] the SCO transition is only detectable through SQUID magnetometry for thicknesses above 40 nm (~60 LPE cycles). Hence, in this work we have tried to maximize the signal-to-noise ratio by fabricating 90-cycles films. The analysis of the AFM scratching measurements reveals thicknesses of 65.7 ± 6.3 nm and 100.7 ± 8.9 nm for thin films of FePymPt and FeIsoqPt, respectively. This is in good agreement with that expected for an axial LbL growth taking into account the c parameter of the unit cell (SI Figure S10). The structural characteristics of the films were studied by GIXRD. Comparison between the experimental and simulated out-of-plane diffractograms (Figure 6a, b) unveils that the films display the same structure than that of the corresponding single crystals with the metal-cyanide layers oriented parallel to the Au substrate. Thus, our experiments confirm the crystallinity and preferential orientation of the films as consistent with our previous work for ultrathin films.[30] Next, the chemical nature of the thin films was also analyzed with XPS measurements. First, the spectra of both films show the constitutive elements of FePymPt and FeIsoqPt (SI Figure S11). Furthermore, as observed in Figure 6c and d, the high-resolution spectra of the Fe 2p and Pt 4f regions of the films and bulk samples obtained for the FePymPt and FeIsoqPt based systems are in very good agreement and consistent with the corresponding N 1s and C 1s spectra (SI Figure S12). Besides, Fe/Pt ratio values for thin films of Pym and Isoq, calculated from peak area integration, 1.3 and 1.1, respectively, are very close to the theoretical value of 1 and very similar to the bulk ratios (1.2 and 1.1, respectively). All these observations suggest a high chemical purity of the deposited thin films. Finally, the films' surface topology was analyzed by AFM. Figure 6e and f display representative images of 10 × 10 and 1 × 1 μm^2 areas of the FePymPt and FeIsoqPt films, respectively. The calculated RMS roughness values are 7.2 ± 1.3 nm and 7.4 ± 1.1 nm, showing a high homogeneity of the obtained films across micrometric-scale areas.

SCO Properties of Thin Films. The thermal evolution of the SCO properties was monitored through SQUID magnetometry for 90-cycles thin films of FePymPt and FeIsoqPt, which were grown onto diamagnetic Mylar/Ti/Au (15 nm) substrates. For comparative reasons, we will also include the 60-cycles thin films of the homologous FePyPt derivative whose raw magnetic properties were previously reported.[29] In order to get significant signal-to-noise ratios, several identically prepared square thin film pieces of ca. 0.5 cm^2 were measured simultaneously for the three compounds applying a magnetic field of 0.1 T. The thermal dependence of the raw magnetization (M) was characterized by a dominant diamagnetic signal mainly belonging to the substrate. However, the signature of the SCO behavior was clearly detected by the presence of a characteristic deflection in the M vs T plot, thereby denoting the spin state change of the deposited film. Aiming at estimating the relevant parameters of the SCO, the experimental magnetization corrected from the diamagnetic component of the substrate was simulated (M_{sim}) using eq 1:

$$M_{sim} = \left[\frac{\gamma_{HS}\cdot(\chi_M T)^{HS}}{T}\right]\frac{H\cdot m}{Mw} + C \quad (1)$$

where γ_{HS} is the thermal dependence of the HS molar fraction, $(\chi_M T)^{HS}$ is the $\chi_M T$ value of the compound in the HS state, T is the temperature, H is the applied magnetic field, m and Mw are the mass of material deposited on the substrate and its molecular weight, respectively, and C is a correction factor. The values of T and γ_{HS} are related through the Slichter−Drickamer mean-field model as follows:[34−36]

$$T = \frac{T_{1/2}\cdot\Delta S + \Gamma\cdot(1 + \gamma_{HS}^{R} - 2\gamma_{HS})}{\Delta S + R\cdot\ln\left[\frac{1-\gamma_{HS}}{\gamma_{HS}-\gamma_{HS}^{R}}\right]} \quad (2)$$

where $T_{1/2}$ is the characteristic temperature at which $\gamma_{HS} = \gamma_{LS} = 0.5$ (i.e., where the Gibbs free energy is zero), ΔS is the entropy variation, Γ the parameter accounting for cooperativity, γ_{HS}^{R} is an inconvertible γ_{HS} fraction and R the universal constant of gases.

The experimental and simulated thermal dependence of M and $\chi_M T$ product for FePyPt, FePymPt, and FeIsoqPt are shown in Figure 7. The inferred thermodynamic parameters, gathered in Table 1, are consistent with those obtained for similar cooperative SCO transitions in Fe^{II}−HCPs.[19] It is worthwhile mentioning that, for FePyPt, the value of γ_H^R perfectly agrees with that previously reported from analysis of the thermal dependence of XAS spectra for the same thin film sample.[29] This fact, together with the satisfactory agreement between experimental and calculated data for FePyPt, validates the analysis of the SCO properties for the homologous FePymPt and FeIsoqPt thin films. However, the asymmetric shape of the FePymPt SCO behavior generates some discrepancy between the γ_H^R values obtained from M vs T (0.53) and $\chi_M T$ vs T (0.57). The masses of compound estimated from the magnetic measurements are 2.45×10^{-5}, 1.19×10^{-4} and 1.85×10^{-4} g for FePyPt, FePymPt, and FeIsoqPt, respectively.

Table 1. Thermodynamic Parameters Obtained from Simulation of the Experimental M vs T curves for FePyPt, FePymPt, and FeIsoqPt

	$T_{1/2}{}^{av}$K	ΔS J/ Kmol	$\Delta H = T_{1/2}{}^{av}\Delta S$ kJ/mol	Γ kJ/mol	γ_{HS}^{R}
FePyPt	199	80	15.92	5.8	0.30
FePymPt	188	77	14.47	6.0	0.57−0.53
FeIsoqPt	129	54	6.97	1.1	0.61

DISCUSSION

Encouraged by the results recently reported on the epitaxial growth of FePyPt thin films,[29] we decided to investigate new closely related compounds derived from the replacement of the Py axial ligand by the Pym and Isoq ligands, both as bulk microcrystalline samples and as nanometric thin films. The primary objective was to assess the influence of small axial ligand modifications on the thin film growth and their consequences on the cooperativity and completeness of the SCO transition.

The resulting FePymM·xH$_2$O and FeIsoqM (M = Ni, Pd, Pt) series here reported join the library of 2D Fe^{II}−HCPs formulated $\{Fe^{II}(L)_2[M^{II}(CN)_4]\}_n$ with L being the pyridine-type ligands Py,[37,38] 3-fluoro and 3-chloropyridine (3Fpy, 3Clpy),[39] 4-phenylpyridine (4Phpy),[40] 4-tetrathiofulvalenylcarboxamidopyridine (ttf−adpy),[41] 4-styrylpyridine (stpy) and 4-(2-phenylethyl)pyridine (pep),[42] 3-aminopyridine (3NH$_2$py),[43] 4-(1H-pyrazol-3-yl)pyridine (Hppy),[44] 2-substituted pyrazines,[45,46] 5-bromopyrimidine (5BrPym),[47] pyridazine (pdz),[48] and phthalazine (Phth).[49]

From a structural point of view, FePymM·xH$_2$O (M = Pd, Pt) are isostructural to their FePyM (M = Ni, Pd, Pt) homologues and share essential structural features with the other members of the $\{Fe^{II}(L)_2[M^{II}(CN)_4]\}_n$ family mentioned above. In contrast, the strongly corrugated $\{Fe[Ni(CN)_4]\}_n$ layers in FePymNi favors the axial coordination of the Ni atom by the "free" N atom of one interdigitated Pym axial ligand belonging to the adjacent layer, thereby changing its coordination geometry from square planar to square based pyramid thus affording a 3D coordination polymer.

At variance with FePyM (M = Ni, Pd, Pt) and despite the efficient packing of the layers, the presence of the "free" N atom in the FePymM·xH$_2$O (M = Pd, Pt) derivatives facilitates the inclusion of a labile H$_2$O molecule, which is stabilized through hydrogen bonding. Although the anhydrous FeIsoqM (M = Ni, Pd, Pt) series crystallize in a different space group, they display the same packing of layers as the pyridine (M = Ni, Pd, Pt) and pyrimidine (M = Pd, Pt) analogues. As most compounds of the $\{Fe^{II}(L)_2[M^{II}(CN)_4]\}_n$ family, the FePymM·xH$_2$O [M = Pd (x = 0, 1), Pt (x = 0, 0.5, 1)] and FeIsoqM [M = Pd, Pt] derivatives display complete one-step abrupt cooperative thermal-induced spin transitions at ambient pressure. In contrast, the corresponding Ni^{II} (x = 0) derivatives remain in HS in the measured temperature range at ambient pressure. However, they show cooperative hysteretic SCO behavior at higher pressures. The lack of SCO in FePymNi at room pressure contrasts with the homologous FePdzNi·H$_2$O (pdz = pyridazine) compound whose layers are planar and shows a hysteretic SCO centered at 224 K.[48] Clearly, the strong corrugation and, especially, the uncommon axial coordination of the Ni atom strongly coupling the layers most probably generate important elastic frustration in FePymNi.

Compounds FePymM·xH$_2$O [M = Pd (x = 1), Pt (x = 1, 0.5)] are strictly isomorphous and differences in their SCO properties are marginal, particularly if we compare the Pd (x = 1) and Pt (x = 0.5) derivatives. The most significant difference between the Pd (x = 1) and Pt (x = 1) derivatives occurs in the $T_{1/2}{}^{\downarrow}$ value (cooling branch), which is 10 K smaller for the latter, thus, making the corresponding hysteresis wider. Complete dehydration has opposite effects, $T_{1/2}{}^{av}$ increases from 222 K (x = 1) up to 237 K (x = 0) for M = Pt, while it decreases from 223 K (x = 1) down to 206 K (x = 0) for M = Pd. In both derivatives, the water molecule is loosely attached and desorbs upon gentle heating. Consequently, the observed impact of 15−20 K on $T_{1/2}{}^{av}$ upon complete desorption can be considered small. These results are consistent with those reported for the homologous FePdzM·xH$_2$O (M = Pd, Pt), whose hydrated forms (x = 1) display rather incomplete SCO behaviors featuring unsymmetrical hysteresis loops centered at $T_{1/2}{}^{av}$ = 253.5 K (Pd) and 245 K (Pt). Upon dehydration (x = 0) the SCO becomes complete and the hysteresis more regular with $T_{1/2}{}^{av}$ virtually being the same for M = Pd but increasing 31 K for M = Pt (276 K).

Rationalization of the sign of $T_{1/2}{}^{av}$ and $\Delta T_{1/2}$ changes in SCO is often a difficult task to accomplish. Although the SCO is in origin a molecular phenomenon, its manifestation is modulated by solid-state effects derived from the texture of each particular material. It is experimentally well established that subtle factors such as size of crystallites, crystallinity degree, amorphousness,

etc., influence $T_{1/2}^{av}$, $\Delta T_{1/2}$ and the molar fraction of inactive HS centers. In the present case, during the process of dehydration these factors may evolve differently for the Pd and Pt derivatives affecting differently the SCO. In this respect, the elastic properties of the solid play a pivotal role in the SCO properties ($T_{1/2}^{av}$ and $\Delta T_{1/2}$).[50] Indeed, the cooperative properties as well as the variation of the ligand field strength felt by the SCO centers due to the positive or negative chemical pressure induced by the lattice are directly proportional to the bulk modulus, which in turn is directly proportional to the density (ρ) of the material ($B = \rho[\partial\rho/\partial p]^{-1}$, p is pressure). It is obvious that for the isostructural $\{Fe(L)_2[M(CN)_4]\}$ series with M = Ni, Pd, and Pt, ρ increases when moving from Ni to Pt. For example, ρ is ca. 15% larger for FePymPt·0.5H_2O than FePymPd·1H_2O and a similar value is observed for FeIsoqM (M = Pd, Pt). Then, it is expected that B would experience a parallel increase somehow attenuated by the term $[\partial\rho/\partial p]^{-1}$, which for low pressures should not differ significantly along the isomorphous series, at least for small pressures. Consequently, in absence of other dominant factors, the $T_{1/2}^{av}$ values for the {Fe(L) [M-(CN)$_4$]} series should increase with B, a fact observed for several families of 2D SCO Hofmann clathrates.

The significantly smaller $T_{1/2}^{av}$ values found for FeIsoqM [180.5 K (Pd) and 165.0 K (Pt)] cannot be justified by electronic effects since the N-donor atom of Isoq has the same basicity as Py and much larger than Pym.[51] This observation can be correlated with the large variation of the layer's corrugation, and hence of the tilt angle defined by the axial ligands, upon spin state change in both Isoq derivatives. In addition, these synchronized events are responsible for the very small, but significant, observed compaction between layers upon LS↔HS transformation. The larger size of the axial Isoq ligand and its more extended aromatic nature compared with Pym and related pyridine derivatives seem to be the ultimate reasons. In the LS state, the Isoq ligands of adjacent layers are strongly interacting essentially via $\pi-\pi$ forces, although there are also short contacts with the C atoms of the CN groups (see SI Figure S13 and SI Table S6). In the HS state, some of these contacts disappear with the expansion of the unit cell but still remain an important number of strong attractive $\pi-\pi$ interactions and one relevant contact with the CN groups, which seem to be the driving force of the strong tilt angle and corrugation changes of the layers upon SCO. In contrast, although the LS state of the Pym derivatives displays some interlayer contacts, which are weaker than those found in the Isoq derivatives, they completely vanish in the HS state (SI Table S6). Consequently, the $\pi-\pi$ extended interactions in FeIsoqM (M = Pd, Pt) act as strong glue between the layers in the LS state and persist in the HS state preventing the Isoq ligands to adopt a more relaxed position, namely a smaller tilt angle. As a result, the Fe−C−N(cyanide) bond angle is forced to change from 175.3° in the LS state to 162.8° in the HS state, a fact synchronized with the strong increase of corrugation in the layers, which are responsible for the decrease in the interlayer separation and much smaller $\Delta V_{SCO}/V_{HS}$ variation with respect to the Pym derivatives (see movie in SI). The latter fact is clearly reflected on the relatively small ΔS variation (55.1 and 60.5 J·K^{-1}·mol^{-1} Pt and Pd, respectively) with respect to the Pym homologous (74.0 and 70.8 J·K^{-1}·mol^{-1} Pd and Pt, respectively). It is worth mentioning that the major contribution to ΔS comes from the change of frequency of molecular and crystal phonon modes which are strongly dependent on the unit cell change upon SCO.[32,39] Obviously, all the structural reorganization observed in the Isoq derivatives is also reflected in the smaller values of enthalpy involved and, consequently, in the smaller $T_{1/2} = \Delta H/\Delta S$ values. These observations agree well with the results recently reported for the homologous Pd and Pt phthalazine derivatives.[49] Both ligands are practically equal in size and consequently the change of unit cell volume, ΔH^{av} and ΔS^{av} are similar. The most important difference is found in the degree of corrugation of the layers in the LS state which is 53% larger in the phthalazine derivatives. Another important difference concerns the number of $\pi-\pi$ contacts, which is markedly larger in the HS state for the Isoq derivatives, thereby justifying their much larger hysteresis loops.

The LPE method enabled us the elaboration of thin films of FePymPt and FeIsoqPt whose chemical identity, epitaxial orientation and high crystallinity have been confirmed by XPS and GIXRD. Based on our previous experience in trying to detect the SCO transition on the films trough SQUID measurements for FePyPt, the thickness of the films was fixed at 90 deposited layers. According to the crystal parameters and in good agreement with the AFM measurements, this corresponds to a thickness of ca. 60 and 100 nm for 90 layers of both FePymPt and FeIsoqPt, respectively. The thermal dependence of the magnetization confirmed the occurrence of SCO behavior for both derivatives. In an effort to extract quantitative SCO information from the 90-cycles FePymPt and FeIsoqPt and 60-cycles FePyPt thin films, simulation of the M vs T curves (corrected from the substrate signal) allowed to get reasonable $\chi_M T$ vs T curves and thermodynamic parameters. The results show obvious effects on the SCO properties when moving from bulk single crystals to thin film samples. For example, the amount of Fe^{II} centers that become SCO inactive and remain in HS at low temperatures (γ_{HS}^{R}) increases progressively from FePyPt (30%), to FePymPt (55%) and FeIsoqPt (61%). Simultaneously, $T_{1/2}^{av}$ decreases by 38, 49, and 36 K for Py, Pym and Isoq derivatives respectively, while the corresponding hysteresis width displays a disparate evolution, decreasing ca. 18 K, from 44 to 26 K for FePyPt, increasing 9 K from 18 to 27 K for FePymPt and decreasing ca. 38 K, practically disappearing for FeIsoqPt. The increase of γ_{HS}^{R} together with the decrease in $T_{1/2}$ are effects usually observed when downsizing the thickness of films or the dimensions of nanocrystals.[54−58] In nanocrystals, the rapid increase of the surface/volume ratio with size decrease is the source of a great number of defects, essentially, at the periphery where the Fe^{II} centers usually complete the axial coordination with a terminal molecule of solvent, thereby drastically decreasing the ligand field strength and increasing γ_{HS}^{R}. The growth of thin films using the LbL method is subjected of considerable "mosaicity" as it was shown for FePyPt,[29] in strong contrast with the ideal image of a homogeneous surface that this method may intuitively transmit. Indeed, for FePyPt, below a threshold of ca. 15-cycles the layer's mosaicity consists of evenly distributed "stalagmitic-like" independent nanorods (ca. 26 nm wide). This imprints a discontinuous character to the film, it is the source of defects and is responsible for the exponential increase of γ_{HS}^{R} as the number of growth cycles decreases. However, above this threshold, coalescence of the nanorods affords more compact homogeneous films characterized by a value of $\gamma_{HS}^{R} \approx 0.3$ which remains practically constant according to XAS measurements.[19]

The present analysis of the thermal dependence of magnetization for 60 cycles films of FePyPt perfectly agrees with the HS fraction mentioned above. This γ_{HS}^{R} value is behind a decrease in cooperativity of ca. 14.7% from $\Gamma_{HS} = 6.8$ kJ mol^{-1} ($\gamma_{HS}^{R} \approx 0.03$) for the bulk microcrystalline sample (see SI Figure S14) to 5.8 kJ

mol^{-1} as estimated for the films. The same analysis shows that γ_{HS}^{R} is markedly larger for the films FePymPt (≈ 0.55) and FeIsoqPt (≈ 0.6) suggesting that an optimal degree of coalescence is attained for a much larger number of layers, thus increasing the level of defects in the film. Indeed, for the Isoq derivative the effects on cooperativity are dramatic since the hysteresis loop practically disappears; Γ decreases in about 78% from 5.0 kJ mol^{-1} (bulk sample, see SI Figure S14) to 1.1 kJ mol^{-1} (thin film). In spite of having a close γ_{H}^{R} value, the films of FePymPt display a relatively wide hysteresis loop, which is rather asymmetric. The simulation of the experimental data gives a value of Γ ≈ 6.0 kJ mol^{-1}, which is just only ca. 5% smaller than the one calculated for the SCO of the bulk crystalline material (Γ ≈ 6.3 kJ mol^{-1} see SI Figure S14). This value is clearly overestimated and should be seen as the largest Γ value observed in the films. Asymmetric hysteresis loops are generally associated with a vast distribution of crystallite sizes spreading from micro to nanometric scale featuring a distribution of different $T_{1/2}^{av}$ and $\Delta T_{1/2}$ parameters and conferring to the SCO a less abrupt shape, as it is the present case. A comparable situation in the films would be associated with an inhomogeneous distribution of the mosaicity defined by nanorods of different dimensions. Furthermore, the size of the "stalagmitic" nanorods seems to be the cause of the respective persistence and loss of hysteresis loop in FePymPt and FeIsoqPt. In order to check this, we processed AFM topography images of both 90-cycles films with a Prewitt operator that highlights particle edges.[59,60] Indeed, a comparison between them clearly shows that these nanoparticles are noticeable larger for FePymPt (SI Figure S15).

CONCLUSION

In summary, here we have described the crystal structure, magnetic and calorimetric properties of two new series of 2D Fe^{II}–HCP with strong cooperative thermal and pressure driven SCO properties. Our improved LPE methodology previously applied to elaborate thin films of the homologous compound FePyPt, has been transferred to two of them, FePymPt and FeIsoqPt. The SCO properties of 90-cycles films of these compounds and 60-cycles films of FePyPt have been assessed through magnetic measurements on a SQUID magnetometer, showing that it is possible to monitor the SCO behavior for films containing a deposited mass in the 2 × 10^{-5}-2 × 10^{-4} g interval. Our results confirm that, when processed as thin films, the reported compounds show SCO at lower temperatures than the corresponding microcrystalline samples. Furthermore, whereas the FePyPt films retain interesting cooperative and reasonably complete SCO properties, a noticeable increase of inactive HS Fe^{II} centers is observed for FePymPt and FeIsoqPt inducing a complete loss of cooperativity for the latter compound and an asymmetric hysteresis loop for the former. This study shows that despite the great structural resemblance of the three compounds, their preparation as thin films follows different growth mechanism that dramatically affect their SCO properties. Therefore, these findings should serve as a cautionary tale for further work with films of other SCO systems grown via LbL.

EXPERIMENTAL SECTION

Materials. *Materials and Reagents.* Iron(II) tetrafluoroborate hexahydrate ($Fe(BF_4)_2{\cdot}6H_2O$), pyrimidine (Pym), isoquinoline (isoq), 4-mercaptopyridine (py-SH) (TCI, > 97%), tetrabutylammonium bromide (TBABr), potassium tetracyanoplatinate(II) hydrate [$K_2Pt(CN)_4{\cdot}xH_2O$] potassium tetracyanopalladate(II) hydrate and potassium tetracyanonickelate(II) were obtained from commercial sources and used as received without further purification. Anhydrous ethanol (99.5%) was purchased from Acros Organics. Other solvents (HPLC-grade) were purchased from Scharlab S.L. (TBA)$_2$Pt(CN)$_4$ was synthesized following a literature procedure.[61] The synthesis of the corresponding complexes was carried out as follows:

Synthesis of FePymM·xH$_2$O; M = Ni (x = 0), Pd (x = 1) and Pt (x = 1). Single crystals were obtained through slow liquid-to-liquid diffusion methods using a 10 mL-total volume H-shaped tube. One arm of the tube was filled with 1 mL of a solution containing a mixture of 28 mg of $Fe(BF_4)_2{\cdot}6H_2O$ (0.1 mmol) and 20 mg (0.25 mmol) of pyrimidinein 2 mL of water whereas the other one was filled with an aqueous solution (1.5 mL) of 43/37/24 mg (0.1 mmol) of $K_2[M(CN)_4]$ (M = Pt^{II}/Pd^{II}/Ni^{II}). The rest of the tube was carefully filled with a methanol:water (1:1) solution, closed with parafilm and left to stand at room temperature. Light yellow cubic single crystals of FePymPt·H$_2$O and FePymPd·H$_2$O were obtained after 2 weeks and the dehydrated counterparts obtained by treating the samples at 400 K during (yield ~55%). Besides, FePymNi crystallizes as dark yellow cubic plates within 3–4 weeks (yield ~60%). *Elemental Analysis*: Calculated for FePymPt·0.5H$_2$O[$C_{12}H_9FeN_8O_{0.5}Pt$ (523.99) (%)]: C 27.50; H 1.73; N 21.38. Found (%): C 27.18; H 1.68; N 21.13. Calculated for dehydrated FePymPd[$C_{12}H_8FeN_8Pd$ (425.93) (%)]: C 33.79; H 1.89; N 26.27. Found (%): C 33.28; H 1.72; N 26.06. Calculated for FePymNi[$C_{12}H_8FeN_8Ni$ (377.96) (%)]: C 38.05; H 2.13; N 14.74. Found (%): C 38.17; H 2.23; N 14.36.

Synthesis of FeIsoqM (M = Ni, Pd, Pt). Single crystals of the isoquinoline based compounds were obtained through slow liquid-to-liquid diffusion methods. One arm of the H-tube was filled with 1 mL of a solution containing 28 mg of $Fe(BF_4)_2{\cdot}6H_2O$ (0.1 mmol) and the other extreme of the tube was filled with a mixture of 43/37/24 mg (0.1 mmol) of $K_2[M(CN)_4]$ (M= Pt^{II}/Pd^{II}/Ni^{II}) and 32 mg (0.25 mmol) of isoquinolinein a methanol:water (1:2) solution (1.5 mL). The rest of the tube was carefully filled with a methanol:water (1:1) solution, closed with parafilm and leaved at room temperature. Yellow square-shaped thin plates of FeIsoqPt, FeIsoqPd, or FeIsoqNi were obtained after 2 weeks (yield: 62%). *Elemental Analysis*: Calculated for FeIsoqPt [$C_{22}H_{14}FeN_6Pt$ (613.33) (%)]: C 43.08; H 2.30; N 13.70. Found (%): C 42.79; H 2.24; N 13.20. FeIsoqPd [$C_{22}H_{14}FeN_6Pd$ (523.97) (%)]: C 50.36; H 2.69; N 16.02. Found (%): C 50.64; H 2.51; N 15.92. FeIsoqNi [$C_{22}H_{14}FeN_6Ni$ (476.00) (%)]: C 55.40; H 2.96; N 17.62. Found (%): C 55.06; H 2.78; N 17.98.

Physical Measurements. *Magnetic Measurements.* Variable-temperature magnetic susceptibility data were recorded with a Quantum Design MPMS2 SQUID magnetometer equipped with a 7 T magnet, operating at 1 T and at temperatures 1.8–400 K. Experimental susceptibilities were corrected for diamagnetism of the constituent atoms by the use of Pascal's constants. Mylar was used as a diamagnetic substrate for thin film measurements.

Calorimetric Measurements. DSC measurements were performed using a differential scanning calorimeter Mettler Toledo DSC 821e. Low temperatures were obtained with an aluminum block attached to the sample holder, refrigerated with a flow of liquid nitrogen and stabilized at a temperature of 110 K. The sample holder was kept in a drybox under a flow of dry nitrogen gas to avoid water condensation. The measurements were carried out using around 15 mg of microcrystalline samples of FePymPt, FePymPd, FeIsoqPt, or FeIsoqPd sealed in aluminum pans with a mechanical crimp. Temperature and heat flow calibrations were made with standard samples of indium by using its melting transition (429.6 K, 28.45 J·g^{-1}). An overall accuracy of ±0.2 K in temperature and ±2% in the heat capacity is estimated. The uncertainty increases for the determination of the anomalous enthalpy and entropy due to the subtraction of an unknown baseline.

Powder X-ray Diffraction (PXRD) Measurements. PXRD analysis were performed on a PANalytical Empyrean X-ray powder diffractometer (monochromatic CuKα radiation, 1.5418 Å). Patterns were collected from polycrystalline powders using a high-throughput screening platform in transmission mode, with the diffractometer operating at 40 mA and 45 kV and using a PIXcel detector. Profiles were collected by using a Soller Slit of 0.02° and a divergence slit of $^1/_4$ at

room temperature in the angular range $3° < 2\theta < 50°$ with a step size of 0.013°.

Elemental CHN Analysis. CHN analysis was performed using a FlashSmart (Thermofisher) elementary analyzer with a thermal conductivity detector. Helium and oxygen (both purity 99.995%) were used as the carrier and combusting gases, respectively. The combustion tube was set up at 950 °C, and the reduction tube was set up at 600 °C. Sulfanilamide was used as CHNS standard.

Single Crystal X-ray Diffraction. Single-crystal X-ray data were collected on an Oxford Diffraction Supernova diffractometer using graphite monochromated Mo$K\alpha$ radiation (λ = 0.71073 Å). A multiscan absorption correction was performed. The structures were solved by direct methods using SHELXS-2014 and refined by full-matrix least-squares on F^2 using SHELXL-2014.[62] Non-hydrogen atoms were refined anisotropically and hydrogen atoms were placed in calculated positions refined using idealized geometries (riding model) and assigned fixed isotropic displacement parameters. CCDC 1910989 ($FePymPt\cdot 0.5H_2O$ in LS), 1910992 ($FePymPt\cdot 0.5H_2O$ in HS), 1989158 ($FePymPd\cdot 1H_2O$ in LS), 1989157 ($FePymPd\cdot 1H_2O$ in HS), 1989159 (FePymNi), 1910991 (FeIsoqPt in LS), 1910990 (FeIsoqPt in HS), 1989161 (FeIsoqPd in LS), 1989162 (FeIsoqPd in HS), and 1989160 (FeIsoqNi) contain the supplementary crystallographic data for this article. These data can be obtained free of charge from The Cambridge Crystallographic Data Centre via www.ccdc.cam.ac.uk/data_request/cif.

Substrate Preparation and SAM Functionalization. Prior to Au evaporation, substrates were soaked in a freshly prepared solution of $H_2O_2/NH_4OH/H_2O$ (1:1:2) and sonicated for 10 min. This treatment was repeated three times. Next, they were rinsed with Milli-Q water, sonicated 5 min in Milli-Q water twice, and dried under a stream of N_2. Then, 3 nm of Ti followed by 15 nm of Au were evaporated using an Edwars Auto 500 thermal evaporator placed inside a N_2-filled glovebox. The base pressure and evaporation rate were 2×10^{-6} mbar and 0.2 Å·s^{-1}, respectively. For self-assembled monolayer (SAM) functionalization, Au substrates were previously activated via O_2 plasma treatment (MiniPCFlecto, Plasma Technology) and then immersed in a 1 mM ethanol solution of py-SH for 24h. Next, substrates were rinsed with fresh ethanol and dried under a stream of N_2.

LPE Fabrication of $[Fe(L)_2\{Pt(CN)_4\}]$ Ultrathin Films. Films were prepared according to the reported methodology. Au substrates functionalized with a py-SH SAM were sequentially immersed in anhydrous ethanol solutions of 25 mM $Fe(BF_4)_2$/100 mM L and 25 mM $(TBA)_2Pt(CN)_4$/100 mM L with intermediate pure anhydrous ethanol washings steps. The immersion times were 3 min in each solution and 1 min in pure anhydrous ethanol. The LPE sequential immersion was performed using a KSV automatic dipping system placed in a N_2-filled glovebox at room temperature. After the final intended number of immersion cycles was completed, substrates were dried under a stream of N_2.

Atomic Force Microscopy. Measurements were performed with a Digital Instruments Veeco Nanoscope IVa microscope in tapping mode using Si tips with a natural resonance frequency of 300 kHz and with an equivalent constant force of 40 N·m^{-1}. The scan rate was adjusted during the scanning of each image and kept in between 0.1 and 1 Hz. Resolution for all images was 512 points/line. Film thickness was evaluated by scratching off the Fe^{II}–HCP film using a soft pointy tool.

X-ray Photoelectron Spectroscopy. Spectra were collected at the X-ray spectroscopy Service of the Universitat d'Alacant using a K-Alpha X-ray photoelectron spectrometer system (Thermo Scientific). All spectra were collected using Al Kα radiation (1486.6 eV), monochromatized by a twin crystal monochromator, yielding a focused X-ray spot (elliptical in shape with a major axis length of 400 μm) at 3 mA·C and 12 kV. The Alpha hemispherical analyzer was operated in the constant energy mode with survey scan pass energies of 200 eV to measure the whole energy band and 50 eV in a narrow scan to selectively measure the particular elements. X-ray photoelectron spectroscopy (XPS) data were analyzed with Avantage software. A smart background function was used to approximate the experimental backgrounds. Charge compensation was achieved with the system flood gun that provides low energy electrons and low energy argon ions from a single source. Spectra were referenced using the C 1s main peak (285.0 eV).

Grazing incidence X-ray diffraction (GIXRD). Thin film diffractograms were collected with a PANalytical Empyrean diffractometer operating at 40 mA and 45 kV using copper radiation (Cu Kα = 1.5418 ÅÅ) and a PIXcel 1D detector in scanning line mode. Single scans were acquired in Bragg–Brentano geometry ($\Omega = 2°$) using a Soller Slit of 0.02°, a divergence slit of $^1/_2$ and an antiscatter slit of $^1/_{16}$ at room temperature in the angular range $2\theta = 4°–40°$ with a step size of 0.026°.

ASSOCIATED CONTENT

*

Figure S1. Powder X-ray diffraction patterns of FePymM and FeIsoqM; Figure S2. Thermal analysis for $FePymPt\cdot 0.5H_2O$ and FePymPd; Figure S3. Clausius–Clapeyron plot for FePymNi and FeIsoqNi; Table S1. Data obtained from the magnetic measurements; Figure S4. DSC curves for $FePymPt\cdot 0.5H_2O$, FePymPd (dehydrated form) and FeIsoqM (M = Pd, Pt); Table S2. Crystal data for FePymM (M = Ni, Pd, Pt); Table S3. Crystal data for FeIsoqM (M = Ni, Pd, Pt); Table S4. Selected bond lengths and angles for FePymM (M = Ni, Pd, Pt); Figure S5. Fragment of the crystal structure of $FePymPt\cdot 0.5H_2O$; Figure S6. Thermal dependence of the unit cell volume for $FePymPt\cdot 0.5H_2O$ and $FePymPd\cdot 1H_2O$; Figure S7. Powder X-ray diffraction patterns of $FePymPt\cdot xH_2O$ (x = 0.5 or 0) and $FePymPd\cdot xH_2O$ (x = 1 or 0); Figure S8. Topological reduction of the FePymNi framework; Table S5. Selected bond lengths and angles for FeIsoqM structures; Figure S9. superposition of the coordination environments of FeIsoqM (M = Pd, Pt) in the HS and LS states; Figure S10. AFM topographic images and height distribution of FePymPt and FeIsoqPt thin films; Figure S11. Survey XPS spectra of FePymPt and FeIsoqPt thin films; Figure S12. High-resolution XPS spectra of the N 1s and C 1s regions of FePymPt and FeIsoqPt thin films; Figure S13. C···C intermolecular contacts for FeIsoqPt and $FePymPt\cdot 0.5H_2O$; Table S6. Interlayer short contacts for FeIsoqPt and $FePymPt\cdot 0.5H_2O$; Figure S14. Simulation of the SCO behavior for bulk microcrystalline samples of FePyPt, FePymPt and FeIsoqPt; Figure S15. Prewitt images of 90-cycles films of FePymPt and FeIsoqPt (PDF)

Structural changes of the FeIsoqPt compound when switching between the HS and the LS configurations (MOV)

AUTHOR INFORMATION

Corresponding Authors

Carlos Bartual-Murgui – *Instituto de Ciencia Molecular (ICMol), Universitat de València, 46980 Paterna, Spain;* orcid.org/0000-0003-1547-8018; Email: carlos.bartual@uv.es

José Antonio Real – *Instituto de Ciencia Molecular (ICMol), Universitat de València, 46980 Paterna, Spain;* orcid.org/0000-0002-2302-561X; Email: jose.a.real@uv.es

Authors

Víctor Rubio-Giménez – *Instituto de Ciencia Molecular (ICMol), Universitat de València, 46980 Paterna, Spain;* orcid.org/0000-0003-1269-5885

Manuel Meneses-Sánchez − *Instituto de Ciencia Molecular (ICMol), Universitat de València, 46980 Paterna, Spain*
Francisco Javier Valverde-Muñoz − *Instituto de Ciencia Molecular (ICMol), Universitat de València, 46980 Paterna, Spain*
Sergio Tatay − *Instituto de Ciencia Molecular (ICMol), Universitat de València, 46980 Paterna, Spain;* orcid.org/0000-0003-0785-866X
Carlos Martí-Gastaldo − *Instituto de Ciencia Molecular (ICMol), Universitat de València, 46980 Paterna, Spain;* orcid.org/0000-0003-3203-0047
M. Carmen Muñoz − *Departamento de Física Aplicada, Universitat Politécnica de València, E-46022 Valencia, Spain;* orcid.org/0000-0003-2630-3897

Complete contact information is available at: https://pubs.acs.org/10.1021/acsami.0c05733

Author Contributions

The manuscript was written through contributions of all authors.

Notes

The authors declare no competing financial interest.

ACKNOWLEDGMENTS

We thank the Spanish Ministerio de Economía y Competitividad (MINECO) and FEDER funds (CTQ2016-78341-P, CTQ2017-83486-P, RTI2018-098568-A-100 and Unidad de Excelencia María de Maeztu MDM-2015-0538), Generalitat Valenciana (PROMETEO/2016/147) and EU Framework FET-OPEN project COSMICS (grant agreement 766726) and ERC Stg Chem-fs-MOF (714122). S.T. thanks the Ramon y Cajal Fellowship (RYC-2016-19817). V.R.-G. thanks the Spanish Ministerio de Ciencia, Innovación y Universidades (MCIU) for his FPU (FPU13/03203) predoctoral fellowship. FJVM and MMS thank MINECO for a predoctoral FPI grant. The atomic spectroscopy section of SCSIE (Universitat de València) is gratefully acknowledged for the Elemental CHNSO analysis. We also thank Francisco Palazón for his assistance with GIXRD measurements and Alejandra Soriano-Portillo and Ángel López-Muñoz for their technical support.

REFERENCES

(1) Manrique-Juárez, M. D.; Rat, S.; Salmon, L.; Molnár, G.; Quintero, C. M.; Nicu, L.; Shepherd, H. J.; Bousseksou, A. Switchable Molecule-based Materials for Micro-and Nanoscale actuating Applications: Achievements and prospects. *Coord. Chem. Rev.* 2016, *308*, 395−408.

(2) Kumar, K. S.; Ruben, M. Sublimable Spin Crossover Complexes: from Spin-state Switching to Molecular Devices. *Angew. Chem., Int. Ed.* 2019. DOI: 10.1002/ange.201911256.

(3) Kõnig, E. Nature and Dynamics of the Spin-state Interconversion in Metal Complexes. *Struct. Bonding (Berlin, Ger.)* 1991, *76*, 51−152.

(4) Gütlich, P.; Hauser, A.; Spiering, H. Thermal and Optical Switching of Iron(II) Complexes. *Angew. Chem., Int. Ed. Engl.* 1994, *33*, 2024−2054.

(5) Real, J. A.; Gaspar, A. B.; Niel, V.; Muñoz, M. C. Communication between Iron(II) building Blocks in Cooperative Spin Transition Phenomena. *Coord. Chem. Rev.* 2003, *236*, 121−141.

(6) Gütlich, P.; Goodwin, G. Spin Crossover in Transition Metal Compound I-III. *Top. Curr. Chem.* 2004, *235*, 233−235.

(7) Real, J. A.; Gaspar, A. B.; Muñoz, M. C. Thermal, Pressure and Light Switchable Spin-Crossover Materials. *Dalton Trans.* 2005, 2062−2079.

(8) Bousseksou, A.; Molnár, G.; Salmon, L.; Nicolazzi, W. Molecular Spin Crossover Phenomenon: Recent Achievements and Prospects. *Chem. Soc. Rev.* 2011, *40*, 3313−3335.

(9) *Spin-crossover Materials: Properties and Applications*, Halcrow, M. A., Ed.; Wiley & Sons Ltd, 2013.

(10) Bousseksou, A.; Molnár, G.; Demont, P.; Menegotto, J. Observation of a Thermal Hysteresis Loop in the Dielectric Constant of Spin Crossover Complexes: Towards Molecular Memory Devices. *J. Mater. Chem.* 2003, *13*, 2069−2071.

(11) Lefter, C.; Davesne, V.; Salmon, L.; Molnár, G.; Demont, P.; Rotaru, A.; Bousseksou, A. Charge Transport and Electrical Properties of Spin Crossover Materials: Towards Nanoelectronic and Spintronic Devices. *Magnetochemistry* 2016, 2 (18), 1−19.

(12) Guionneau, P.; Marchivie, M.; Bravic, G.; Letard, J.-F.; Chasseau, D. Structural Aspects of Spin Crossover. Example of the [Fe^{II}Ln(NCS)$_2$] Complexes. *Top. Curr. Chem.* 2004, *234*, 97−128.

(13) Collet, E.; Guionneau, P. Structural Analysis of Spin-Crossover Materials: From Molecules to Materials. *C. R. Chim.* 2018, *21*, 1133−1151.

(14) Akou, A.; Gural'Skiy, I. A.; Salmon, L.; Bartual-Murgui, C.; Thibault, C.; Vieu, C.; Molnár, G.; Bousseksou, A. Soft Lithographic Patterning of Spin Crossover Complexes. Part 2: Stimuli-Responsive Diffraction Grating Properties. *J. Mater. Chem.* 2012, *22*, 3752−3757.

(15) Bartual-Murgui, C.; Akou, A.; Thibault, C.; Molnár, G.; Vieu, C.; Salmon, L.; Bousseksou, A. Spin-Crossover Metal-organic Frameworks: Promising Materials for Designing Gas Sensors. *J. Mater. Chem. C* 2015, *3*, 1277−1285.

(16) Kahn, O. Spin-Transition Polymers: From Molecular Materials Toward Memory Devices. *Science* 2002, *279*, 44−48.

(17) Molnar, G.; Rat, S.; Salmon, L.; Nicolazzi, W.; Bousseksou, A. Spin Crossover Nanomaterials: From Fundamental Concepts to Devices. *Adv. Mater.* 2018, *30* (1−23), 17003862.

(18) Kumar, K. S.; Ruben, M. Emerging Trends in Spin Crossover (SCO) Based Functional Materials and Devices. *Coord. Chem. Rev.* 2017, *346*, 176−205.

(19) Muñoz, M. C.; Real, J. A. Thermo-, Piezo-, Photo- and Chemo-Switchable Spin Crossover Iron(II)-Metallocyanate Based Coordination Polymers. *Coord. Chem. Rev.* 2011, *255*, 2068−2093.

(20) Ni, Z.-P.; Liu, J.-L.; Hoque, N., Md.; Liu, W.; Li, J.-Y.; Chen, Y.-C.; Tong, M.-L. Recent Advances in Guest Effects on Spin-Crossover Behavior in Hofmann-type Metal-Organic Frameworks. *Coord. Chem. Rev.* 2017, *335*, 28−43.

(21) Otsubo, K.; Haraguchi, T.; Kitagawa, H. Nanoscale Crystalline Architectures of Hofmann-Type Metal-organic Frameworks. *Coord. Chem. Rev.* 2017, *346*, 123−138.

(22) Bell, C. M.; Arendt, M. F.; Gomez, L.; Schmehl, R. H.; Mallouk, T. E. Growth of Lamellar Hofmann Clathrate Films by Sequential Ligand Exchange Reactions: Assembling a Coordination Solid One Layer at a Time. *J. Am. Chem. Soc.* 1994, *116*, 8374−8375.

(23) Cobo, S.; Molnár, G.; Real, J. A.; Bousseksou, A. Multilayer Sequential Assembly of Thin Films That Display Room-Temperature Spin Crossover with Hysteresis. *Angew. Chem., Int. Ed.* 2006, *45*, 5786−5789.

(24) Otsubo, K.; Haraguchi, T.; Sakata, O.; Fujiwara, A.; Kitagawa, H. Step-by-Step Fabrication of a Highly Oriented Crystalline Three-Dimensional Pillared-Layer-Type Metal-Organic Framework Thin Film Confirmed by Synchrotron X-Ray Diffraction. *J. Am. Chem. Soc.* 2012, *134*, 9605−9608.

(25) Bartual-Murgui, C.; Salmon, L.; Akou, A.; Thibault, C.; Molnár, G.; Mahfoud, T.; Sekkat, Z.; Real, J. A.; Bousseksou, A. High Quality Nano-Patterned Thin Films of the Coordination Compound {Fe(Pyrazine)[Pt(CN)4]} Deposited Layer-by-Layer. *New J. Chem.* 2011, *35*, 2089−2094.

(26) Bartual-Murgui, C.; Akou, A.; Salmon, L.; Molnár, G.; Thibault, C.; Real, J. A.; Bousseksou, A. Guest Effect on Nanopatterned Spin-Crossover Thin Films. *Small* 2011, *7*, 3385−3391.

(27) Agustí, G.; Cobo, S.; Gaspar, A. B.; Molnár, G.; Moussa, N. O.; Szilagyi, P. Á.; Pálfi, V.; Vieu, C.; Muñoz, M. C.; Real, J. A. Thermal and Light-Induced Spin Crossover Phenomena in New 3D Hofmann-Like

Microporous Metalorganic Frameworks Produced As Bulk Materials and Nanopatterned Thin Films. *Chem. Mater.* 2008, *20*, 6721−6732.

(28) Sakaida, S.; Otsubo, K.; Sakata, O.; Song, C.; Fujiwara, A.; Takata, M.; Kitagawa, H. Crystalline Coordination Framework Endowed with Dynamic Gate-Opening Behaviour by Being Downsized to a Thin Film. *Nat. Chem.* 2016, *8*, 377−383.

(29) Rubio-Gimen□ez, V.; Bartual-Murgui, C.; Galbiati, M.; Nu□ez Lop□ez, A.; Castells-Gil, J.; Quinard, B.; Seneor, P.; Otero, E.; Ohresser,
P.; Cantarero, A.; et al. Effect of Nanostructuration on the Spin Crossover Transition in Crystalline Ultrathin Films. *Chem. Sci.* 2019, *10*, 4038−4047.

(30) Rubio-Gimen□ez, V.; Escorcia-Ariza, G.; Bartual-Murgui, C.; Sternemann, C.; Galbiati, M.; Castells-Gil, J.; Real, J. A.; Tatay, S.; Martí-Gastaldo, C. Ultrathin Films of 2D Hofmann-Type Coordination Polymers: Influence of Pillaring Linkers on Structural Flexibility and Vertical Charge Transport. *Chem. Mater.* 2019, *31*, 7277−7287.

(31) Gaspar, A. B.; Molnar□, G.; Rotaru, A.; Shepherd, H. J. Pressure effect investigations on spin crossover coordination compounds. *C. R. Chim.* 2018, *21*, 1095−1120.

(32) Öhrström, L.; Larsson, K. *Molecule-Based Materials, The structural Network Approach*; Elsevier: Amsterdam, The Nederlands, 2005.

(33) Liu, Q.; Li, Y. Z.; Song, Y.; Liu, H. J.; Xu, Z. Three-Dimensional Five-connected Coordination Polymer $[M_2(C_3H_2O_4)_2(H_2O)_2((2\text{-}hmt)]_n$ with 4^46^6 Topologies (M = Zn, Cu; hmt = hexamethylenetetramine). *J. Solid State Chem.* 2004, *177*, 4701−4705.

(34) Slichter, C. P.; Drickamer, H. G. Pressure-induced Electronic Changes in Compounds of Iron. *J. Chem. Phys.* 1972, *56*, 2142−2160.

(35) Martin, J. P.; Zarembowitch, J.; Bousseksou, A.; Dworkin, A.; Haasnoot, J. G.; Varret, F. Solid State Effects on Spin Transitions: Magnetic, Calorimetric, and Mossbauer-Effect Properties of $[Fe_xCo_{1x}(4,4'\text{-bis-1,2,4-triazole})_2(NCS)_2]\eta H_2O$ Mixed-Crystal Compounds. *Inorg. Chem.* 1994, *33*, 6325−6333.

(36) Martin, J. P.; Zarembowitch, J.; Dworkin, A.; Haasnoot, J. G.; Codjovi, E. Solid-State Effects in Spin Transitions: Role of Iron(II) dilution in the magnetic and calorimetric properties of the series $[Fe_xNi_{1-x}(4,4'\text{-bis(1,2,4-triazole)})_2(NCS)_2]\eta H_2O$. *Inorg. Chem.* 1994, *33*, 2617−2623.

(37) Kitazawa, T.; Gomi, Y.; Takahashi, M.; Takeda, M.; Enemoto, M.; Miyazaki, A.; Enoki, T. Spin-Crossover Behavior of the Coordination Polymer $Fe^{II}(C_5H_5N)_2Ni^{II}(CN)_4$. *J. Mater. Chem.* 1996, *6*, 119−121.

(38) Niel, V.; Martinez-Agudo, J. M.; Mun□oz, M. C.; Gaspar, A. B.; Real, J. A. Cooperative Spin Crossover Behavior in Cyanide-Bridged Fe(II)-M(II) Bimetallic 3D Hofmann-like Networks (M = Ni, Pd, and Pt). *Inorg. Chem.* 2001, *40*, 3838−3839.

(39) Martínez, V.; Gaspar, A. B.; Mun□oz, M. C.; Bukin, G. V.; Levchenko, G.; Real, J. A. Synthesis and Characterisation of a New Series of Bistable Iron(II) Spin-Crossover 2D Metal-Organic Frameworks. *Chem. - Eur. J.* 2009, *15*, 10960−10971.

(40) Seredyuk, M.; Gaspar, A. B.; Ksenofontov, V.; Verdaguer, M.; Villain, F.; Gütlich, P. Thermal- and Light-Induced Spin Crossover in Novel 2D Fe(II) Metalorganic Frameworks $\{Fe(4\text{-}PhPy)_2[M^{II}(CN)_x]_y\}\eta sH_2O$: Spectroscopic, Structural, and Magnetic Studies. *Inorg. Chem.* 2009, *48*, 6130−6141.

(41) Martínez, V.; Gaspar, A. B.; Mun□oz, M. C.; Ballesteros, R.; Ortega-Villar, N.; Ugalde-Saldívar, V. M.; Moreno-Esparza, R.; Real, J. A. Spin-Crossover 2D Metal-Organic Frameworks with a Redox-Active Ligand: $[Fe(Ttf\text{-}Adpy)_2M(CN)_4]\eta nH_2O$ (Ttf-Adpy = 4-Tetrathiafulvalenylcarboxamidopyridine; M^{II} = Ni, Pd, Pt). *Eur. J. Inorg. Chem.* 2009, *2009*, 303−310.

(42) Ohtani, R.; Arai, M.; Ohba, H.; Hori, A.; Takata, M.; Kitagawa, S.; Ohba, M. Modulation of the Interlayer Structures and Magnetic Behavior of 2D Spin-Crossover Coordination Polymers $[Fe^{II}(L)_2Pt^{II}(CN)_4]$. *Eur. J. Inorg. Chem.* 2013, *2013*, 738−744.

(43) Liu, W.; Wang, L.; Su, Y. J.; Chen, Y. C.; Tucek, J.; Zboril, R.; Ni, Z. P.; Tong, M. L. Hysteretic Spin Crossover in Two-Dimensional (2D) Hofmann-Type Coordination Polymers. *Inorg. Chem.* 2015, *54*, 8711−8716.

(44) Liu, F. L.; Tao, J. Hysteretic Two-Step Spin-Crossover Behavior in Two Two-Dimensional Hofmann-Type Coordination Polymers. *Chem. - Eur. J.* 2017, *23*, 18252−18257.

(45) Valverde-Mun□oz, F. J.; Seredyuk, M.; Mun□oz, M. C.; Znovjyak, K.; Fritsky, I. O.; Real, J. A. Strong Cooperative Spin Crossover in 2D and 3D Fe^{II}-$M^{I, II}$ Hofmann-Like Coordination Polymers Based on 2-Fluoropyrazine. *Inorg. Chem.* 2016, *55*, 10654−10665.

(46) Kucheriv, O. I.; Shylin, S. I.; Ksenofontov, V.; Dechert, S.; Haukka, M.; Fritsky, I. O.; Guralskiy, I. A. Spin Crossover in Fe(II)-M(II) Cyanoheterobimetallic Frameworks (M = Ni, Pd, Pt) with 2-Substituted Pyrazines. *Inorg. Chem.* 2016, *55*, 4906−4914.

(47) Agustí, G.; Gaspar, A. B.; Mun□oz, M. C.; Real, J. A. Thermal- and Pressure-Induced Cooperative Spin Transition in the 2D and 3D Coordination Polymers $\{Fe(5\text{-}Br\text{-}pmd)_z[M(CN)_x]_y\}$ (M = Ag^I, Au^I, Ni^{II}, Pd^{II}, Pt^{II}). *Inorg. Chem.* 2007, *4* (6), 9646−9654.

(48) Gural′skiy, I. A.; Shylin, S. I.; Ksenofontov, V.; Tremel, W. Pyridazine-Supported Polymeric Cyanometallates with Spin Transitions. *Eur. J. Inorg. Chem.* 2019, *2019*, 4532−4537.

(49) Hiiuk, V. M.; Shova, S.; Rotaru, A.; Golub, A. A.; Fritsky, I. O.; Gural′skiy, I. A. Spin Crossover in 2D Iron(II) Phthalazine Cyanometallic Complexes. *Dalton Trans.* 2020, *49*, 5302−5311.

(50) Spiering, H. Elastic Interaction in Spin-Crossover Compounds. In: Spin Crossover in Transition Metal Compounds III. *Top Curr. Chem.* 2004, *235*, 171−195.

(51) Raczyn□ska, E. D.; Gal, J.-F.; Maria, P.-C. Gas-phase basicity of aromatic azines: A short review on structural effects. *Int. J. Mass Spectrom.* 2017, *418*, 130−139.

(52) Fultz, B. *Phase Transitions in Materials*, 2nd ed.; Cambridge University Press, 2020; pp 209−211.

(53) Molnar, G.; Mikolasek, M.; Ridier, K.; Faks, A.; Nicolazzi, W.; Bousseksou, A. Molecular Spin Crossover Materials: Review of the Lattice Dynamical Properties. *Ann. Phys.* 2019, *531*, 531.

(54) Coronado, E.; Galan□-Mascaros□, J. R.; Monrabal-Capilla, M.; García-Martínez, J.; Pardo-Iban□ez, P. Bistable Spin-Crossover Nanoparticles Showing Magnetic Thermal Hysteresis near Roon Temperatura. *Adv. Mater.* 2007, *19*, 1359−1361.

(55) Boldog, I.; Gaspar, A. B.; Martínez, V.; Pardo-Iban□ez, P.; Ksenofontov, V.; Bhattacharjee, A.; Gütlich, P.; Real, J. A. Spin-Crossover Nanocrystal with Magnetic, Optical, and Structural Bistability near Room Temperature. *Angew. Chem., Int. Ed.* 2008, *47*, 6433−6437.

(56) Volatron, F.; Catala, L.; Rivie□re, E.; Gloter, A.; Stephan, O.; Mallah, T. Spin-Crossover Coordination Nanoparticles. *Inorg. Chem.* 2008, *47*, 6584−6586.

(57) Larionova, J.; Salmon, L.; Guari, Y.; Tokarev, A.; Molvinger, K.; Molnar, G.; Bousseksou, A. Towards the Ultimate Size Limit of the Memory Effect in Spin-Crossover Solids. *Angew. Chem., Int. Ed.* 2008, *47*, 8236−8240.

(58) Martínez, V.; Boldog, I.; Gaspar, A. B.; Ksenofontov, V.; Bhattacharjee, A.; Gütlich, P.; Real, J. A. Spin Crossover Phenomenon in nanocrystals and nanoparticles of $[Fe(3\text{-}Fpy)_2M(CN)_4]$ (M^{II} = Ni, Pd, Pt) Two-Dimensional Coordination Polymers. *Chem. Mater.* 2010, *22*, 4271−4281.

(59) Nečas, D.; Klapetek, P. Gwyddion: an Open-Source Software for SPM Data Analysis. *Cent. Eur. J. Phys.* 2012, *10*, 181−188.

(60) *Picture Processing and Psychopictorics*; Lipkin, B. S., Ed., 1970; pp 75−149.

(61) Mason, W. R., III; Gray, H. B. Electronic Structures of Square-Planar Complexes. *J. Am. Chem. Soc.* 1968, *90*, 5721−5729.

(62) Sheldrick, G. M. Crystal Structure Refinement with SHELXL. *Acta Crystallogr., Sect. C: Struct. Chem.* 2015, *71*, 3−8.